An Explicit One-Dimensional Time-Dependent Tilting Cloud Model

SHU-HUA CHEN

Department of Land, Air, and Water Resources, University of California, Davis, Davis, California

WEN-YIH SUN

Department of Earth and Atmospheric Sciences, Purdue University, West Lafayette, Indiana

(Manuscript received 12 November 2003, in final form 1 June 2004)

ABSTRACT

An explicit one-dimensional time-dependent tilting cloud model has been developed for use in cumulus parameterizations. The tilting axis is not necessarily orthogonal to the (r, θ) plane, making the horizontal axisymmetric assumption more reasonable. This explicit time-dependent tilting model (ETTM) consists of an updraft and a downdraft, which are governed by the same dynamic and thermodynamic equations. The updraft is initiated by a moist thermal bubble, while the downdraft is consequently induced by evaporative cooling and the drag force of precipitation separating from the tilting updraft instead of being arbitrarily initialized.

The updraft is capable of reproducing the major features of a deep cloud such as overshooting cooling above the cloud top, evaporative cooling near the surface, and drying in the lower atmosphere at dissipating stages. The entrainment–detrainment rate in this model is well defined, and its time variation is quite significant. Moreover, the vertical profile of the air inside the updraft does not follow the moist adiabat after deep convection. For the downdraft, the total precipitation and mass flux at low levels contributed from the downdraft cannot be neglected in this case study. In addition, the downdraft can bring dry air from middle levels to lower levels.

Three sensitivity tests—the environmental sounding, the tilting angle, and the radius of the updraft–downdraft—have also been conducted. The cooling–warming of a downdraft near the surface is sensitive to the environmental sounding, consistent with results from Srivastava. The cloud life span, maximum vertical velocity, precipitation amount, and vertical mass flux are strongly influenced by the tilting angle and the radius of the cloud.

The results from the ETTM simulation are quite reasonable and promising. However, some deficiencies of this model still exist, and more research will be conducted to improve its performance. The final goal is to implement this 1D model in a mesoscale model's cumulus parameterization scheme.

1. Introduction

Cumulus parameterization in numerical weather prediction models can significantly affect severe weather forecasts, such as those of hurricanes, flash floods, and winter storms. These severe weather systems are sometimes poorly forecasted, which can lead to increased loss of life and property damage. Therefore, scientists have put much effort into this subject to improve model performance (e.g., Asai and Kasahara 1967; Ooyama 1971; Kuo 1965, 1974; Nitta 1975; Anthes 1977; Arakawa and Schubert 1974; Molinari 1982; Kuo and Raymond 1980; Betts 1986; Tiedtke 1989; Emanuel 1991; Kain and Fritsch 1990, 1993; Grell 1993; Sun and Haines 1996; Wang and Randall 1996; Hu 1997; Grabowski 2001).

Cumulus parameterization schemes consist of three components: triggering functions, the vertical redistribution of thermodynamic and dynamic variables, and closure assumptions (Weather Research and Forecast model development group 5, available online at http://www.wrf-model.org). Triggering functions control the timing and location of subgrid-scale convection. The vertical redistribution of thermodynamic and dynamic variables modifies the large-scale environment, and closure assumptions determine the intensity of convection. All three are very important; however, the emphasis of this study is only related to the issue of the vertical redistribution.

Grell et al. (1991) gave a general review for different approaches for achieving the vertical redistribution of thermodynamic properties (static control and feedback in their paper). In an earlier period, Manabe et al. (1965) and Kuo (1965, 1974) suggested adjusting an unstable layer toward a moist-adiabatic structure through subgrid-scale convection, while Ooyama (1971) and Arakawa and Schubert (1974) introduced an ensemble cloud in a cumulus parameterization scheme. Instead of using a moist adjustment as in Manabe et al. (1965),

Corresponding author address: Shu-Hua Chen, Dept. of Land, Air, and Water Resources, University of California, Davis, Davis, CA 95616-8627.
E-mail: shachen@ucdavis.edu

Betts (1986) suggested that the temperature and moisture should be relaxed to a reference quasi-equilibrium thermodynamic structure, which was based on observational data.

As the resolution of numerical models increases, incorporating a simple plume or bulk one-dimensional (1D) cloud inside a cumulus parameterization scheme to help redistribute thermodynamic and dynamic variables has become more common (e.g., Kreitzberg and Perkey 1976; Anthes 1977; Fritsch and Chappell 1980; Frank and Cohen 1985; Tiedtke 1989; Grell 1993; Hu 1997). With a slightly more sophisticated approach, Kain and Fritsch (1990, 1993) applied an entraining–detraining plume model to the process of cumulus parameterization. However, for efficiency these 1D models were relatively simple and empirical. Grell et al. (1991) commented that a time-dependent, one-dimensional cloud model might be required for a cumulus parameterization scheme in order to get a better estimate of the thermodynamic properties during the life cycle of a cloud.

Liu et al. (2001) used results from a two-dimensional (2D) cloud-resolving model to evaluate the performance of the Kain–Fritsch (KF) scheme. From a numerical study of the Tropical Ocean Global Atmosphere Coupled Ocean–Atmosphere Research Experiment (TOGA COARE), they found that there was a cold bias at the tropopause due to overshooting and a surface cold bias due to the detrainment of downdrafts at the lowest level. Moreover, their simulation results were very sensitive to the magnitude of the moisture detrainment. Liu et al. (2001) concluded that these problems might be due to the simplification of the 1D entrainment plume model.

A few sophisticated 1D cloud models were developed (Ferrier and Houze 1989; Chen and Sun 2002), and some of them have been used in cumulus parameterization (Cheng 1989a; Haines and Sun 1994). Ferrier and Houze (1989) developed a time-dependent 1D model, which included quite complete physical processes, such as vertical mixing, lateral entrainment, pressure perturbation, and warm cloud microphysics. In their model, the radius of the cloud could change with height. The precipitation separating from the updraft due to its tilting effect was considered; however, the downdraft initiated by the evaporative cooling and by the drag force was ignored. Since their model was used to simulate convective systems over the tropical region, the omission of the downdraft and the use of warm rain might be reasonable. In Chen and Sun (2002), their erect 1D cloud tends to generate a convective cloud that is not as deep as that from a 3D model simulation. A similar conclusion was also drawn by Ferrier and Houze (1989). To increase the depth of a convective cloud, they used a cloud radius that decreased with height in the lower atmosphere, and their model was then able to produce a more reasonable cloud depth when compared with observations. It is not surprising to see this result due to the vertical flux effect and because less entrainment occurs in the lower atmosphere when a larger cloud radius is used.

In Cheng's (1989a) 1D tilting cloud model, the updraft–downdraft and detailed entrainment–detrainment effects were included. The importance of the nonhydrostatic pressure has been demonstrated (Holton 1973; Kuo and Raymond 1980; Chen and Sun 2002), but it was ignored in his model. As in Ferrier and Houze (1989), only warm rain processes were considered. Since Cheng's 1D model is a diagnostic cumulus ensemble model, it is more suitable for cumulus parameterization schemes used in coarse-resolution mesoscale and global-scale models. Haines and Sun (1994) developed a quasi-one-dimensional cloud model without the consideration of downdrafts. Their model was time independent and only simple cloud microphysics were used. As the spatial resolution of numerical models increases, the number of clouds within one grid box decreases. As the number of clouds decreases, the effects of convective clouds may become time dependent rather than steady state.

Some details of a 1D cloud model can significantly influence the performance of a cumulus parameterization scheme, such as the downdraft (Brown 1979; Molinari and Corsetti 1985; Cheng 1989b; Grell et al. 1991; Moncrieff 1992; Gray 2000; Liu et al. 2001) and the entrainment–detrainment rate (Arakawa and Schubert 1974; Cheng 1989a). Downdrafts associated with tilting updrafts have often been observed. It is well known that the tilting of a convective cloud is strongly correlated to its environmental wind shear (Moncrieff 1981). The tilting of a convective cloud (or the environmental wind shear) is to take into account the separation of precipitation from its updraft. The separated precipitation can potentially modify the strength and the life span of the updraft (Ferrier and Houze 1989) and, more importantly, might induce a downdraft due to the evaporative cooling and the drag force of the precipitation (Moncrieff 1981). As a consequence, the thermodynamical structure in the boundary layer (low-level heat sink) and the convective momentum transport [in particular the countergradient momentum transport; Moncrieff (1981, 1992)] can be substantially modified by those tilting clouds.

The mass flux of convective clouds can be overestimated in the lower troposphere when downdrafts are not considered. Even if downdrafts are included, their improper representation, such as the level of origin, can also introduce cooling and moistening biases (Liu et al. 2001). Cheng (1989b) found that the apparent heat source–moisture sink and the radiative heating rate from the downdraft are comparable to those from the updraft in the lower troposphere.

Investigating entrainment–detrainment effects, Arakawa and Schubert (1974) hypothesized a constant fractional entrainment rate, defined as the ratio of the entrainment per unit height to the vertical mass flux in the cloud, for each subensemble. They further assumed that entrainment occurred at every level, while detrainment only occurred at the layer near the top of the subensembles. In the study of an erect 1D cloud model,

Chen and Sun (2002) pointed out that the detrainment layer at the upper portion of clouds could be up to 5 km deep, which is more than one layer near the cloud top. It is clear that more realistic entrainment–detrainment rates from the updraft and downdraft are required to reduce temperature, moisture, and momentum biases in cumulus parameterization.

With a quite unique approach, Grabowski (2001) developed a cloud-resolving convection parameterization scheme that was used in a simplified global model. Inspired by Grabowski's work, Khairoutdinov and Randall (2001) developed a superparameterization scheme for the community climate system model. Both schemes embedded a 2D time-dependent cloud model in to a 3D synoptic-scale model in every grid box during the entire simulation period. Their results are quite promising. However, this kind of approach is quite costly in terms of current computational time and memory.

To efficiently and realistically represent the effects of subgrid-scale convective clouds, we develop an explicit 1D time-dependent tilting cloud model for use in cumulus parameterization. One of the purposes of having a tilting updraft is to initiate a downdraft as it was also addressed in Cheng (1989a). This accounts for the subgrid-scale parameterization effects due to the downdraft. The ETTM is dynamically and physically based, and is an improvement to the erect, 1D cloud model in Chen and Sun (2002), which includes an updraft but not a downdraft. In Chen and Sun (2002), the nonhydrostatic pressure perturbation, detailed cloud microphysical processes, entrainment–detrainment effect, lateral eddy mixing, and vertical eddy mixing in a time-dependent erect one-dimensional cloud model were discussed. In this further study, our emphases are on developing a more realistic 1D tilting cloud model and on extending its sophistication by adding the influences of the downdraft, cloud radius, and tilting effects on a cloud. Although a 1D cloud might develop more strongly if the cloud radius changes with height (Ferrier and Houze 1989), we decided to use a constant radius until more evidence is provided from observations or 3D model simulations.

Section 2 illustrates the development of the model, including the details of the downdraft development. The derivations of the governing equations in the tilting coordinates are also demonstrated. Section 3 presents one experiment and its preliminary results. The sensitivity tests of the environmental sounding, tilting angle, and radius of the cloud are shown in section 4. Finally, a brief summary is given in section 5.

2. Model descriptions

a. Coordinate transformation

The governing equations of the ETTM and their symbols in Cartesian coordinates are defined in appendix A. We transform those equations from Cartesian coordinates to general tilting cylindrical coordinates to naturally have the capability of simulating tilting clouds. Figure 1 shows the schematic structure of two coordinates. In the Cartesian coordinates (tilting cylindrical coordinates), $\mathbf{i}$, $\mathbf{j}$, $\mathbf{k}$ ($\mathbf{e}_\theta$, $\mathbf{e}_r$, $\mathbf{e}_z$) and x, y, z (θ, r, Z) are the three basic unit vectors and components. It is well known that the tilting of a cloud is correlated to the environmental wind shear. However, here the tilting angle (α_0), the angle from the vertical axis z to the tilting axis Z, is assumed to be independent of height and is fixed during a cloud life cycle such that the tilting axis lines up with the x axis. Note that the tilting axis Z is not necessarily orthogonal to the (r, θ) plane (more general), as was the case in Cheng (1989a). When the (r, θ) plane is parallel to the (x, y) plane, a horizontally axisymmetric assumption within the cloud is more reasonable. Using this assumption, the horizontal pressure gradient force, for example, can be formulated easily. The relationship of the basic units and components between these two coordinates is expressed as

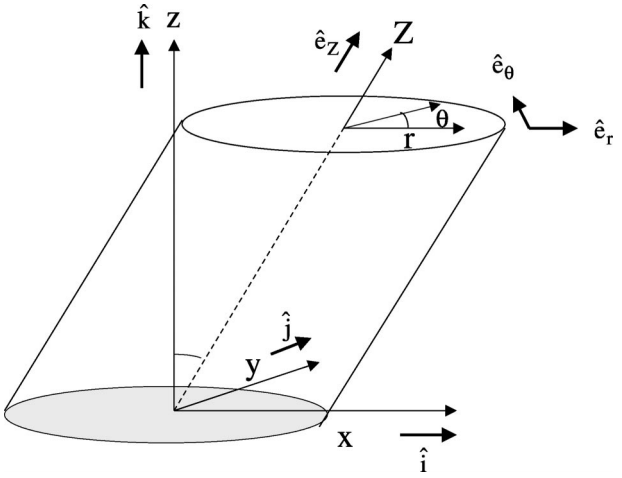

FIG. 1. Structure of the Cartesian coordinates ($\hat{\mathbf{i}}$, $\hat{\mathbf{j}}$, $\hat{\mathbf{k}}$) and the tilting cylindrical coordinates ($\hat{\mathbf{e}}_r$, $\hat{\mathbf{e}}_\theta$, $\hat{\mathbf{e}}_z$).

$$x = r\cos\theta + Z\sin\alpha_0, \qquad y = r\sin\theta,$$
$$z = Z\cos\alpha_0, \tag{1}$$

$$r = \sqrt{(x - az)^2 + y^2}, \qquad \theta = \tan^{-1}\left(\frac{y}{x - az}\right),$$
$$Z = bz, \tag{2}$$

$$\mathbf{i} = \cos\theta\mathbf{e}_r - \sin\theta\mathbf{e}_\theta,$$
$$\mathbf{j} = \sin\theta\mathbf{e}_r + \cos\theta\mathbf{e}_\theta,$$
$$\mathbf{k} = -a\cos\theta\mathbf{e}_r + a\sin\theta\mathbf{e}_\theta + b\mathbf{e}_z, \tag{3}$$

where $a = \tan\alpha_0$ and $b = \sec\alpha_0$, and the relationship of the partial derivatives is

$$\frac{\partial}{\partial x} = \frac{\partial r}{\partial x}\frac{\partial}{\partial r} + \frac{\partial\theta}{\partial x}\frac{\partial}{\partial\theta} + \frac{\partial Z}{\partial x}\frac{\partial}{\partial Z} = \cos\theta\frac{\partial}{\partial r} - \frac{\sin\theta}{r}\frac{\partial}{\partial\theta},$$

$$\frac{\partial}{\partial y} = \sin\theta\frac{\partial}{\partial r} + \frac{\cos\theta}{r}\frac{\partial}{\partial \theta},$$

$$\frac{\partial}{\partial z} = -a\cos\theta\frac{\partial}{\partial r} + a\frac{\sin\theta}{r}\frac{\partial}{\partial \theta} + b\frac{\partial}{\partial Z}. \quad (4)$$

Substituting Eq. (3) into the velocity field yields

$$\begin{aligned}\mathbf{V} &= u\mathbf{i} + v\mathbf{j} + w\mathbf{k}\\ &= u(\cos\theta\,\mathbf{e}_r - \sin\theta\,\mathbf{e}_\theta) + v(\sin\theta\,\mathbf{e}_r + \cos\theta\,\mathbf{e}_\theta)\\ &\quad + w(-a\cos\theta\,\mathbf{e}_r + a\sin\theta\,\mathbf{e}_\theta + b\,\mathbf{e}_z)\\ &= U\mathbf{e}_r + V\mathbf{e}_\theta + W\mathbf{e}_z, \end{aligned} \quad (5)$$

where U, V, and W are radial, tangential, and tilting-axis velocities in the tilting coordinates, respectively, and

$$\begin{pmatrix} U \\ V \\ W \end{pmatrix} = \mathbf{M} \times \begin{pmatrix} u \\ v \\ w \end{pmatrix}. \quad (6)$$

Here, $\mathbf{M}$ is a mapping matrix or a linear operator, and its formula is

$$\mathbf{M} = \begin{pmatrix} \cos\theta & \sin\theta & -a\cos\theta \\ -\sin\theta & \cos\theta & a\sin\theta \\ 0 & 0 & b \end{pmatrix}. \quad (7)$$

b. Governing equations in the tilting cylindrical coordinates

Substituting Eqs. (1), (3), (4), and (5) into the momentum equations [Eqs. (A1)–(A3) in appendix A] results in

$$\begin{aligned}\frac{\partial U}{\partial t} &= -U\frac{\partial U}{\partial r} - \frac{V}{r}\frac{\partial U}{\partial \theta} - W\frac{\partial U}{\partial Z} + \frac{V^2}{r} - \frac{1}{\rho}\frac{\partial p}{\partial r}\\ &\quad - aB\cos\theta - a^2\frac{\cos^2\theta}{\rho}\frac{\partial p_{\rm nh}}{\partial r} + a^2\frac{\cos\theta\sin\theta}{\rho r}\frac{\partial p_{\rm nh}}{\partial \theta}\\ &\quad + ab\frac{\cos\theta}{\rho}\frac{\partial p_{\rm nh}}{\partial Z}, \end{aligned} \quad (8)$$

$$\begin{aligned}\frac{\partial V}{\partial t} &= -U\frac{\partial V}{\partial r} - \frac{V}{r}\frac{\partial V}{\partial \theta} - W\frac{\partial V}{\partial Z} - \frac{VU}{r} - \frac{1}{\rho r}\frac{\partial p}{\partial \theta}\\ &\quad + aB\sin\theta + a^2\frac{\cos\theta\sin\theta}{\rho}\frac{\partial p_{\rm nh}}{\partial r} - a^2\frac{\sin^2\theta}{\rho r}\frac{\partial p_{\rm nh}}{\partial \theta}\\ &\quad - ab\frac{\sin\theta}{\rho}\frac{\partial p_{\rm nh}}{\partial Z}, \end{aligned} \quad (9)$$

$$\begin{aligned}\frac{\partial W}{\partial t} &= -U\frac{\partial W}{\partial r} - \frac{V}{r}\frac{\partial W}{\partial \theta} - W\frac{\partial W}{\partial Z} - \frac{b^2}{\rho}\frac{\partial p_{\rm nh}}{\partial Z} + bB\\ &\quad + ab\frac{\cos\theta}{\rho}\frac{\partial p_{\rm nh}}{\partial r} - ab\frac{\sin\theta}{\rho r}\frac{\partial p_{\rm nh}}{\partial \theta}, \end{aligned} \quad (10)$$

where

$$B = g\left[\frac{\theta_v - \theta_{v0}}{\theta_{v0}} + \left(\frac{R}{C_p} - 1\right)\frac{p_{\rm nh}}{p_0} - Q_T\right].$$

The first four terms on the right-hand side of Eqs. (8) and (9) and the first three terms of Eq. (10) are similar to those in the regular (orthogonal) cylindrical coordinates. In fact, an erect cloud is a special case of the tilting cloud when the tilting angle (α_0) is zero (i.e., no environmental wind shear). In addition to those similar terms, several terms are generated due to the tilting effect, as they are related to a and b, which are functions of α_0.

The current computing requirements make it prohibitive to apply a 3D cloud model for the subgrid-scale cumulus parameterization in a large-scale model. To simplify the problem, we further assume that the cloud is horizontally symmetric with respect to the tilting axis ($\partial/\partial\theta = 0$) within the cloud. With the use of the continuity equation, momentum Eqs. (8)–(10) become

$$\begin{aligned}\frac{\partial U}{\partial t} &= -\frac{1}{r}\frac{\partial(rUU)}{\partial r} - \frac{1}{\rho}\frac{\partial(\rho WU)}{\partial Z} + \frac{V^2}{r} - \frac{1}{\rho}\frac{\partial p}{\partial r}\\ &\quad - aB\cos\theta - a^2\frac{\cos^2\theta}{\rho}\frac{\partial p_{\rm nh}}{\partial r} + ab\frac{\cos\theta}{\rho}\frac{\partial p_{\rm nh}}{\partial Z}, \end{aligned} \quad (11)$$

$$\begin{aligned}\frac{\partial V}{\partial t} &= -\frac{1}{r}\frac{\partial(rUV)}{\partial r} - \frac{1}{\rho}\frac{\partial(\rho WV)}{\partial Z} - \frac{VU}{r} + aB\sin\theta\\ &\quad + a^2\frac{\cos\theta\sin\theta}{\rho}\frac{\partial p_{\rm nh}}{\partial r} - ab\frac{\sin\theta}{\rho}\frac{\partial p_{\rm nh}}{\partial Z}, \end{aligned} \quad (12)$$

$$\begin{aligned}\frac{\partial W}{\partial t} &= -\frac{1}{r}\frac{\partial(rUW)}{\partial r} - \frac{1}{\rho}\frac{\partial(\rho WW)}{\partial Z} - \frac{b^2}{\rho}\frac{\partial p_{\rm nh}}{\partial Z} + bB\\ &\quad + ab\frac{\cos\theta}{\rho}\frac{\partial p_{\rm nh}}{\partial r}. \end{aligned} \quad (13)$$

The same procedure is also applied to other equations, but here only the equation for the precipitation hydrometeors (q_y) is presented (the others are shown in appendix B):

$$\begin{aligned}\frac{\partial q_y}{\partial t} &= -\frac{1}{r}\frac{\partial(rUq_y)}{\partial r} - \frac{1}{\rho}\frac{\partial(\rho Wq_y)}{\partial Z} + R_{\rm in}\frac{b}{\rho}\frac{\partial(\rho V_{\rm ty}q_y)}{\partial Z}\\ &\quad + P_y - \frac{a}{\rho}\cos\theta\frac{\partial(V_{\rm ty}q_y)}{\partial r}, \end{aligned} \quad (14)$$

where $R_{\rm in}$ is the ratio of precipitation that remains in the tilting updraft, while the remaining portion, $(1 - R_{\rm in})$, separates from the updraft and falls into the downdraft (details in section 2d)

c. Horizontal integrations of governing equations

A horizontal integration is performed to reduce the equations from three dimensions to one, similar to the method of Chen and Sun (2002). For any variable A within the cloud, the horizontal area-average value ($\overline{A}$), the deviation from the horizontal average (A'), the lat-

eral boundary average ($\tilde{A}$), and the deviation from the lateral boundary average (A'') are defined as (Asai and Kasahara 1967)

$$\overline{A} = \frac{1}{\pi R^2}\int_0^{2\pi}\int_0^R Ar\, dr\, d\psi,$$

$$A' = A - \overline{A},$$

$$\tilde{A} = \frac{1}{2\pi}\int_0^{2\pi} A\, d\psi,$$

$$A'' = A - \tilde{A}.$$

Following Holton (1973) and Chen and Sun (2002), we assume that the nonhydrostatic pressure perturbation can be expressed as $p_{nh}(r, Z) = p^*(Z)J_0(r)$ in a tilting cloud, where $J_0(r)$ is the zeroth-order Bessel function of the first kind. The radius of the cloud satisfies the first root of $J_0(x) = 0$, where $x = r\alpha/R$ and $\alpha = 2.4048$.

After horizontal averaging, the governing equations become

$$\frac{\partial\overline{D}}{\partial t} = -\frac{2}{R}(\tilde{U}\tilde{D} + \widetilde{U''D''}) - \frac{1}{\rho}\frac{\partial[\rho(\overline{W}\,\overline{D} + \overline{D'W'}]}{\partial Z} - \frac{\overline{D}^2}{2} + \frac{2\alpha}{\rho R^2}J_1(\alpha)\overline{p}^*(Z) + \frac{a^2\alpha}{\rho R^2}J_1(\alpha)\overline{p}^*(Z), \quad (15)$$

$$\frac{\partial\overline{W}}{\partial t} = -\frac{2}{R}(\tilde{U}\tilde{W} + \widetilde{U''W''}) - \frac{1}{\rho}\frac{\partial[\rho(\overline{W}\,\overline{W} + \overline{W'W'})]}{\partial Z} - \frac{2b^2J_1(\alpha)}{\rho\alpha}\frac{\partial\overline{p}^*(\mathrm{Z})}{\partial Z} + bg\frac{\overline{\theta}_v - \theta_{v0}}{\theta_{v0}} - bg\overline{Q}_T + bg\left(\frac{R}{C_p} - 1\right)\frac{2J_1(\alpha)}{\alpha}\frac{\overline{p}^*(\mathrm{Z})}{p_0}, \quad (16)$$

$$\frac{\partial\overline{\theta}_{\mathrm{ei}}}{\partial t} = -\frac{2}{R}(\tilde{U}\tilde{\theta}_{\mathrm{ei}} + \widetilde{U''\theta''_{\mathrm{ei}}}) - \frac{1}{\rho}\frac{\partial[\rho(\overline{W}\,\overline{\theta}_{\mathrm{ei}} + \overline{\theta'_{\mathrm{ei}}W'})]}{\partial Z} + \frac{1}{C_p}(L_v\overline{q}_v - L_f\overline{q}_i)\frac{d}{dt}\left(\frac{\overline{\theta}}{T}\right) + \mathrm{micro}(\overline{\theta}_{\mathrm{ei}}), \quad (17)$$

$$\frac{2}{R}\tilde{U} + \frac{1}{\rho}\frac{\partial(\rho\overline{W})}{\partial Z} = 0, \quad (18)$$

$$\frac{\partial\overline{q}_x}{\partial t} = -\frac{2}{R}(\tilde{U}\tilde{q}_x + \widetilde{U''q''_x}) - \frac{1}{\rho}\frac{\partial[\rho(\overline{W}\,\overline{q}_x + \overline{q'_xW'})]}{\partial Z} + \overline{P}_x, \quad (19)$$

$$\frac{\partial\overline{q}_y}{\partial t} = -\frac{2}{R}(\tilde{U}\tilde{q}_y + \widetilde{U''q''_y}) - \frac{1}{\rho}\frac{\partial[\rho(\overline{W}\,\overline{q}_y + \overline{q'_yW'})]}{\partial Z} + R_{\mathrm{in}}\frac{b}{\rho}\frac{\partial(\rho\overline{V_{\mathrm{ty}}q_y})}{\partial Z} + \overline{P}_y, \quad (20)$$

where $\overline{V}$ is always zero if we assume that initial $\overline{V}$ equals zero and assume that V is horizontally axisymmetric within the cloud. The system in the tilting cylindrical coordinates is similar to that in the orthogonal cylindrical coordinates in Chen and Sun (2002). However, there are three primary differences between these two systems. First, part of the precipitation can separate from the tilting updraft and potentially initiate a downdraft. Second, forcing terms are slightly different between these two systems due to the tilting effect. Third, the total effect of a tilting cloud, which consists of an updraft and a downdraft, is different from that of an erect cloud, which only includes an updraft.

The formulas for the eddy exchange follow Ogura and Takahashi (1971) and Holton (1973). Therefore for any variable A, the parameterization is as follows:

$$\widetilde{U''A''} = \frac{\nu}{R}(\overline{A} - A_o) \quad \text{and} \quad \overline{W'A'} = -K_m\frac{\partial\overline{A}}{\partial Z},$$

where A denotes a momentum variable. If A is a mass variable, K_m is replaced by K_h. The parameters ν, K_m, and K_h are known as the kinematic viscosity of air, momentum eddy coefficient, and heat eddy coefficient, respectively. Following Ogura and Takahashi (1971), the relationship among ν, K_m, and K_h is defined as

$$K_h = \nu = 3K_m = 0.1R|W|. \quad (21)$$

For the updraft, the properties of the environment will be brought into clouds if convergence (or entrainment) occurs, while the properties of clouds will be carried out to the environment if divergence (or detrainment) occurs. For the downdraft, the treatment of the entrainment–detrainment is the same as that in the updraft. However, as mentioned below in section 2d, the detrained air from the updraft can possibly influence the downdraft.

Using Eqs. (15), (16), and (18), the diagnostic equation of the pressure perturbation can be derived as

$$\frac{2b^2J_1}{\alpha}\frac{\partial^2\overline{p}^*(\mathrm{Z})}{\partial Z^2} - bg\left(\frac{R_d}{C_p} - 1\right)\frac{2J_1}{\alpha}\frac{\partial}{\partial Z}\left[\rho\frac{\overline{p}^*(\mathrm{Z})}{p_0}\right] + \frac{(2 + a^2)\alpha}{R^2}J_1\overline{p}^*(\mathrm{Z}) = -\frac{2\rho}{R}(\tilde{U}\tilde{D} + \widetilde{U''D''}) - \frac{\partial}{\partial Z}[\rho(\overline{W}\,\overline{D} + \overline{W'D'})] - \rho\frac{\overline{D}^2}{2} - \frac{2}{R}\frac{\partial}{\partial Z}[\rho(\tilde{U}\tilde{W} + \widetilde{U''W''})] + bg\frac{\partial}{\partial Z}\left(\rho\frac{\overline{\theta}_v - \theta_{vo}}{\theta_{vo}}\right) - \frac{\partial^2}{\partial Z^2}[\rho(\overline{W}\,\overline{W} + \overline{W'W'})] - bg\frac{\partial}{\partial Z}(\rho\overline{Q}_T). \quad (22)$$

The ratios of precipitation remaining inside the updraft (R_{in}), the tilting angle (α_0), and the radius (R) are three parameters that have to be determined in this model. In this study, α_0 and R are given but will be parameterized in the near future. The formula of R_{in} will be discussed in section 2d.

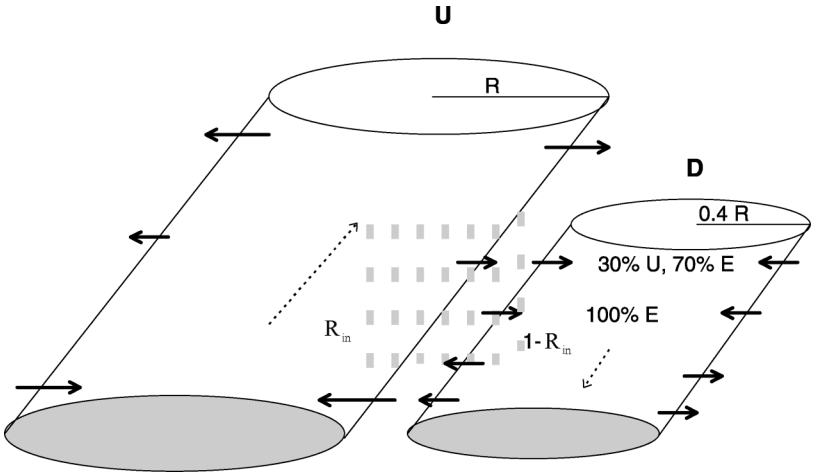

FIG. 2. Schematic structure of the updraft (U) and downdraft (D) in the tilting cloud: E indicates environment and R_{in} is the ratio of precipitation remaining in the updraft. Thick gray dashed lines denote precipitation.

d. Downdraft

When a tilting updraft develops and produces precipitation (rain, snow, or graupel), a portion of the precipitation can separate from the updraft due to the gravitational force if the tilting angle is greater than zero. The separated precipitation can trigger a downdraft (Fig. 2) at the same height. Note that no downdraft exists in this model when the tilting angle is zero. The drag force and the evaporative–sublimative cooling in subsaturated air can enhance the downdraft. The governing equations, tilting angle, and horizontally axisymmetric assumption used in the updraft are applied to the downdraft. However, precipitation does not separate from the downdraft to initiate subsequent downdrafts.

The entrainment–detrainment from the updraft can potentially influence the downdraft. If detrainment occurs in the updraft, and entrainment occurs in the associated downdraft, a maximum of 30% of the detrained air from the updraft can intrude into the downdraft, while the remainder is from the environment. However, if no detrainment occurs in the updraft at that layer, the air entrained into the downdraft comes entirely from the environment (Fig. 2). It is true that the reverse process, in which the updraft is influenced by the downdraft, happens. However, since the radius of the downdraft is assumed to be 40% of the updraft in this study, the influence of the downdraft on the updraft is relatively small and is therefore ignored. Note that the 40% is an approximate value according to the relationship of the diameters between the updraft and downdraft in Lemone and Zipser (1980).

The precipitation that remains inside the updraft is determined by the ratio (R_{in}) of the overlapped volume (or overlapped area) between two tilting columns (or two shaded disks) to the volume of one tilting column (disk) as shown in Fig. 3. The letter A indicates the original precipitation column in the updraft, while A' indicates the column shifted downward with a distance of $H(=V_{ty}\Delta t)$, where V_{ty} is the terminal velocity of precipitation and Δt is the time step. Therefore, R_{in} is defined as

$$R_{in} = \frac{4R^2 \cos^{-1}\left(\frac{H \tan\alpha_0}{2R}\right) - H \tan\alpha_0 \sqrt{4R^2 - H^2 \tan^2\alpha_0}}{2\pi R^2}, \quad (23)$$

where R is the radius of the updraft and the ratio of precipitation falling into the downdraft column is $1 - R_{in}$.

e. Cloud microphysics and numerical method

The microphysics and numerical methods used in both updrafts and downdrafts are the same as those in Chen and Sun (2002). The forward–backward scheme in time (Sun 1984) and the central difference scheme in space are used. The vertical fluxes of precipitation due to terminal velocities are calculated using a forward scheme. Cloud microphysical processes are based on Lin et al. (1983) and Rutledge and Hobbs (1984) with some modifications (Chen and Sun 2002). Details of the

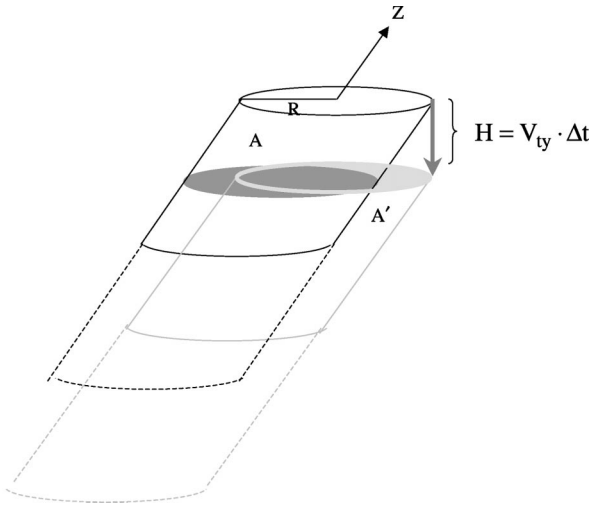

FIG. 3. Schematic diagram of the original precipitation column (A) in the tilting updraft and the column shifted downward (A′) for a distance of H after one time step (Δt) due to the terminal velocity of precipitation (V_{ty}). The radius of the updraft is R.

cloud microphysics and numerical methods are given in Chen and Sun (2002).

3. Experiment and preliminary results

a. Initial conditions

The vertical profiles of the temperature and moisture (thick lines in Fig. 4) from Schlesinger (1978) are used to preliminarily evaluate the performance of the ETTM. This environment is favorable for a severe thunderstorms in the southern Great Plains and has a convective available potential energy (CAPE) of about 3000 J kg^{-1}. A tilting cloud in the ETTM consists of an updraft and a downdraft, and the updraft is initiated using a moist thermal bubble. The formula for the potential temperature perturbation (θ') is given as

$$\theta' = 0.367 \sin\left(\frac{\pi z}{3500}\right), \qquad z \leq 3500 \text{ m},$$

and the relative humidity from 0 to 4.2 km is slightly higher (88%) than that in the environment. The downdraft is then initiated by the precipitation separating from the tilting updraft due to evaporative cooling and the drag force of precipitation instead of being arbi-

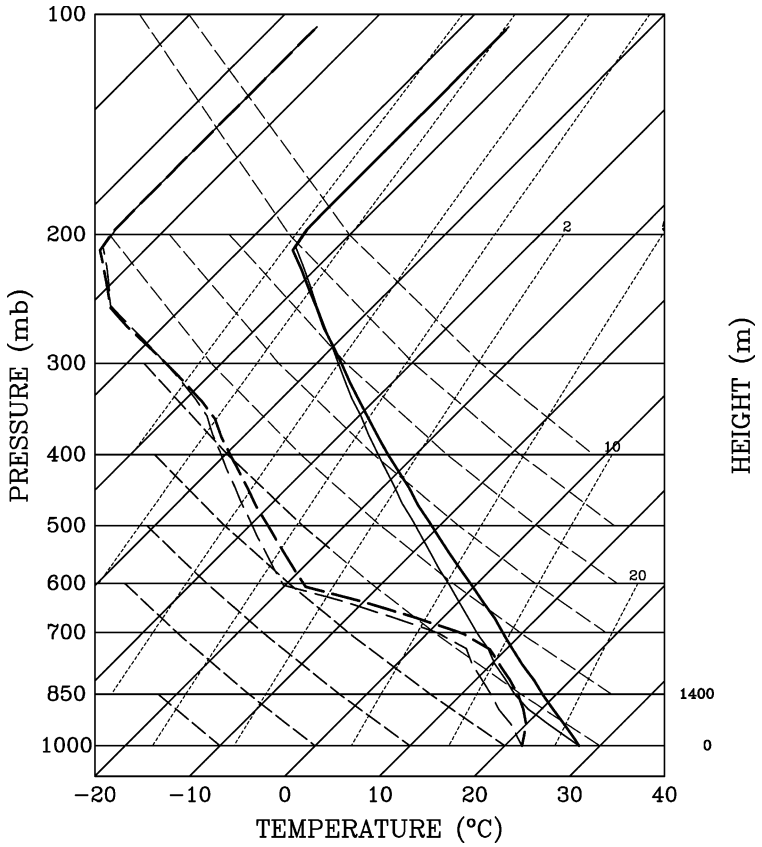

FIG. 4. Skew T–log$p$ diagram of the initial vertical sounding (thick lines) is taken from Schlesinger (1978). The vertical sounding of thin lines is for a sensitivity test. Solid lines are temperatures and long-dashed lines are dewpoints.

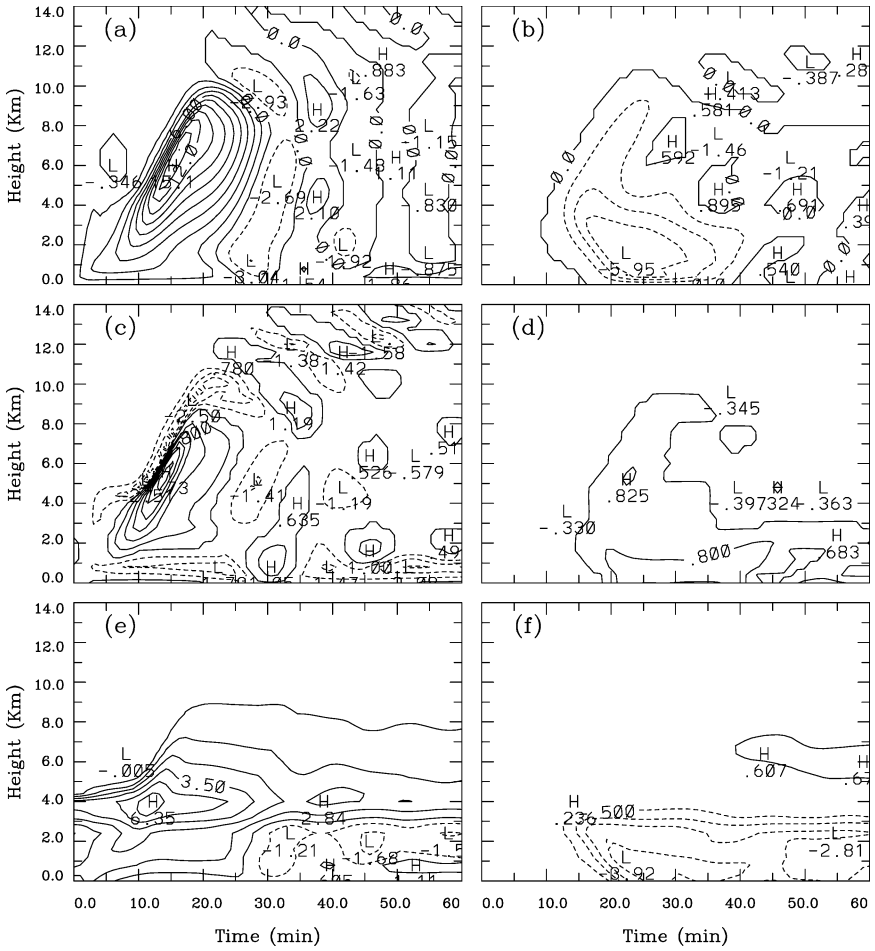

FIG. 5. Time variation of the (a) vertical velocity (m s^{-1}), (c) potential temperature anomaly (K), and (e) moisture anomaly (kg kg^{-1}) from the updraft. (b), (d), (f) The same as in (a), (c), and (e), respectively, except from the downdraft. The values in (e) and (f) are multiplied by 1×10^3.

trarily initialized. The tilting angle is given as 20°, and the radii of the updraft and downdraft are 3000 and 1200 m (40% of the updraft), respectively. The vertical domain is 20 km with a vertical resolution of 400 m. A 5-s time step is used, and the model integrates for 60 min.

b. Results

Figure 5 shows the time variation of the vertical velocity, potential temperature anomaly, and moisture anomaly of the tilting cloud. For the updraft, the maximum upward motion (Fig. 5a), 15.1 m s^{-1}, occurs at 6.4 km after 15 min. The cloud top reaches up to 11 km (cloud field is not shown). After 25 min, downward motion starts replacing upward motion in the lower atmosphere, and eventually the updraft dies at 33 min. A downdraft is initiated by the precipitation separating from the updraft at the height of 4 km after 10 min (Fig. 5b); it then extends up to 9 km, where the strength is much weaker than that at lower levels. The maximum downward motion reaches −5.95 m s^{-1} at 1.2 km, 23 min after the downward motion onset. The life cycles of the updraft (27 min) and downdraft (25 min) in this experiment are quite comparable. Note that a life cycle is measured from the starting point when the absolute vertical velocity reaches a critical value to the end point when this critical value is last maintained. The critical value is 2 m s^{-1} for the updraft but only 1 m s^{-1} for the downdraft, which is generally weaker in the ETTM.

Within the updraft, a maximum potential temperature anomaly, 4.73 K, occurs at 5.6 km at 14 min (Fig. 5c). An overshooting cooling over the cloud top and a cold pool close to the surface are produced. The overshooting cooling reaches its maximum strength (−3.2 K) and depth (2.4 km) after the updraft becomes mature. The surface cold pool is maintained until the updraft dissipates. It has sometimes been observed that the middle-level air penetrating to the ground is colder than the original environment. For the given sounding in Fig. 4 (thick lines), the ETTM produces a warming instead of a cooling in the lower layers of the downdraft (Fig. 5d).

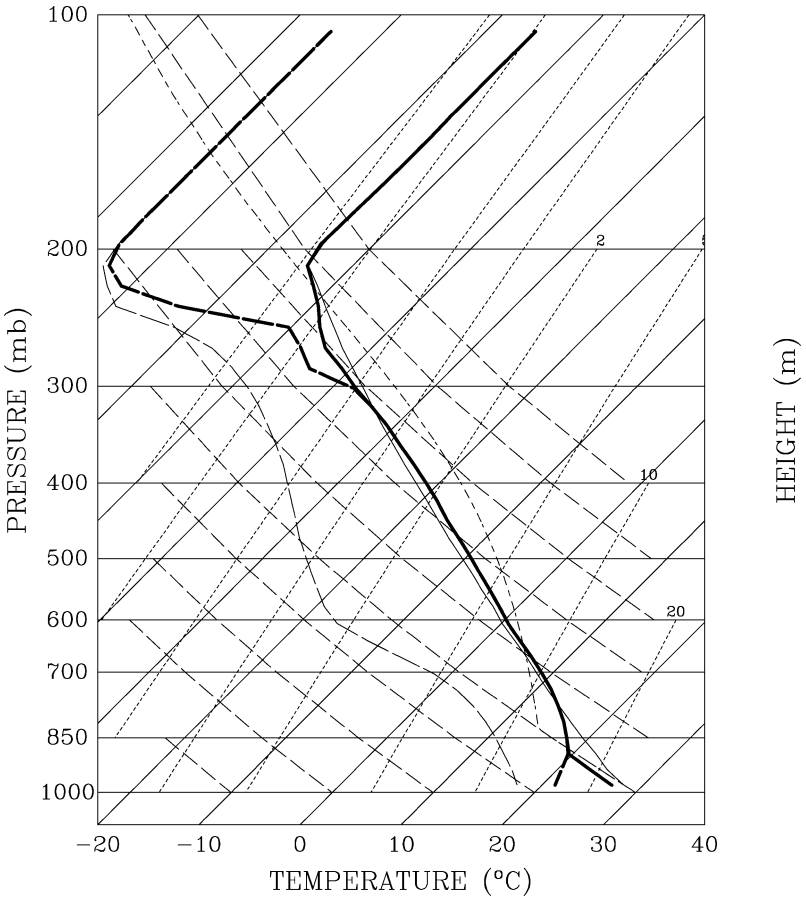

FIG. 6. The skew T–log$p$ diagram of the soundings at 19 min (thick lines) for the updraft and 24 min for the downdraft (thin lines). Solid lines are temperatures and long-dashed lines are dewpoints.

An interpretation and a sensitivity test regarding the issue of cooling–warming are given in section 4.

The updraft column is moistened when low-level moist air is transported upward (Fig. 5e). The maximum anomaly reaches 0.006 35 kg kg^{-1} and occurs at 4 km after 12 min. A drying process in the lower atmosphere is observed within both the downdraft and updraft columns after the downward motion develops. This implies that the moistening rate due to evaporation and sublimation is smaller than the drying rate due to downward advection of dry air, which entrains from middle levels.

Figure 6 shows the skew T–log$p$ diagram of the updraft and downdraft at the time when each of them reaches their maximum heights (19 min for the updraft and 24 min for the downdraft). The air is saturated within the cloudy area in the updraft, while it is unsaturated through the entire column of the downdraft. In the updraft, the temperature profile does not follow a moist adiabat, although it has been convectively adjusted to saturation; this might be due to the involvement of other processes such as entrainment and lateral eddy diffusion. The air below the cloud base is well mixed as both the potential temperature and the mixing ratio of water vapor are near constants. The relative humidity in the updraft is 70% $\sim$ 80%, greater than the 50% $\sim$ 60% in the downdraft due to its strong downward dry advection.

The vertical profiles of relative humidity at 10, 20, and 30 min from the updraft and downdraft are calculated (Fig. 7). In the updraft, the saturated air (cloud) reaches 5 km at 10 min when it is still in the developing stage and reaches 11 km at 20 min. The moisture field drops dramatically immediately above the cloud top. At 30 min the air below 5.2 km within the updraft column becomes subsaturated when the downward motion dominates (Fig. 5a). In the downdraft, the air is subsaturated at all three times. Note that the downdraft column at 10 min, when it is about to develop, can also be treated as the environmental sounding (for comparison purposes). The downdraft column becomes more moist with time than the environment above 4 km. The cloud and precipitation detrained and separated from the updraft are evaporated and sublimated to moisten the upper potion of the downdraft (i.e., compared with the 10-min result), where the downward motion is relatively weak. However, below 4 km, the air becomes drier than the en-

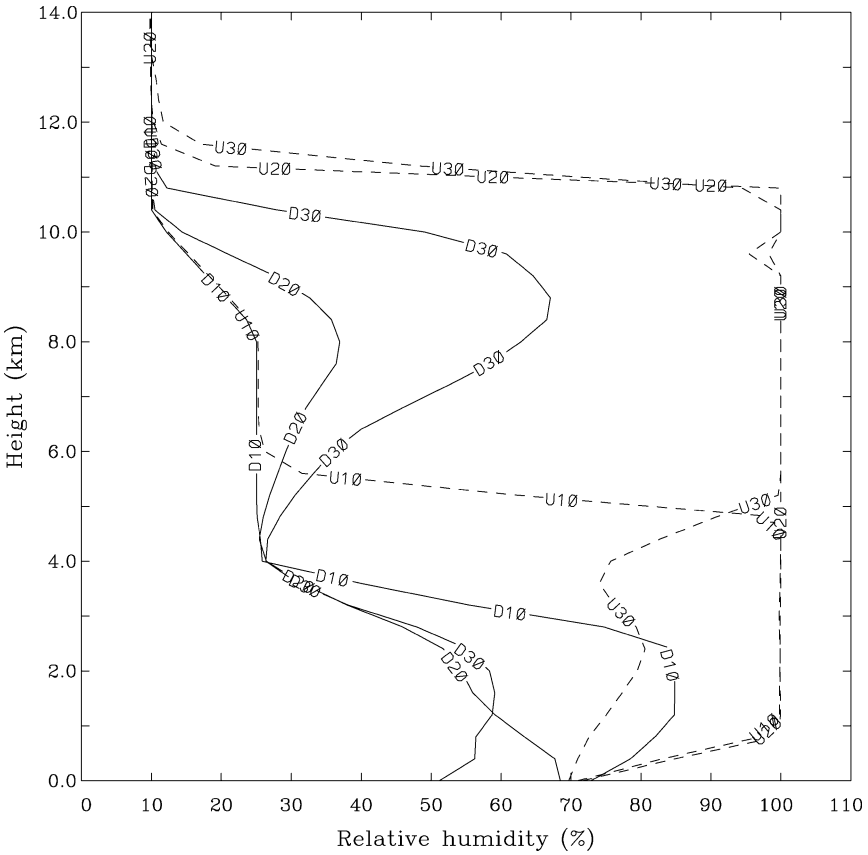

FIG. 7. Vertical profiles of the relative humidity within the updraft at 10 min (dashed line U10), 20 min (dashed line U20), and 30 min (dashed line U30), and within the downdraft at 10 min (line D10), 20 min (line D20), and 30 min (line D30).

vironment due to the strong descent. This is also shown in the updraft column below 2.4 km at 30 min.

The rainfall rate of the tilting cloud is shown in Fig. 8. Rainfall first reaches the ground through the downdraft column and occurs at 15 min. The intensity from the updraft is weaker than that from the downdraft in this experiment. However, the total precipitation amount is larger due to a wider coverage area of the updraft (a 25 to 4 ratio). The maximum downward motion and the maximum rainfall rate in the downdraft occur around the same time (25 min).

A realistic entrainment–detrainment rate is important

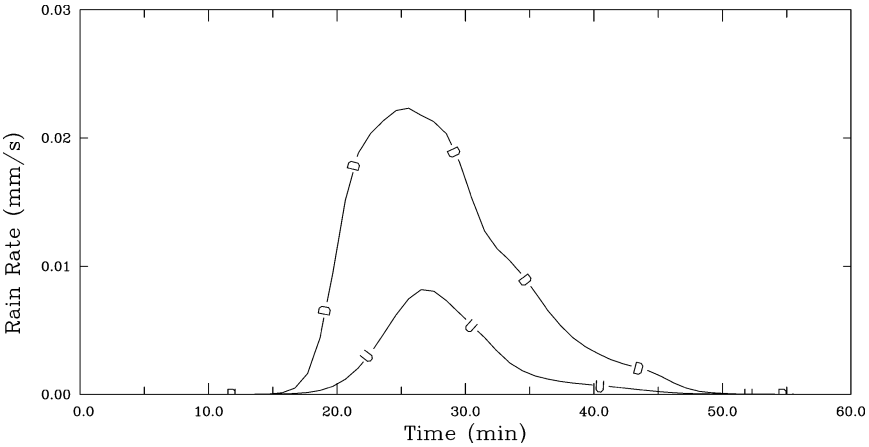

FIG. 8. Time variation of the rainfall rate (mm s^{-1}) from the updraft (line U) and downdraft (line D).

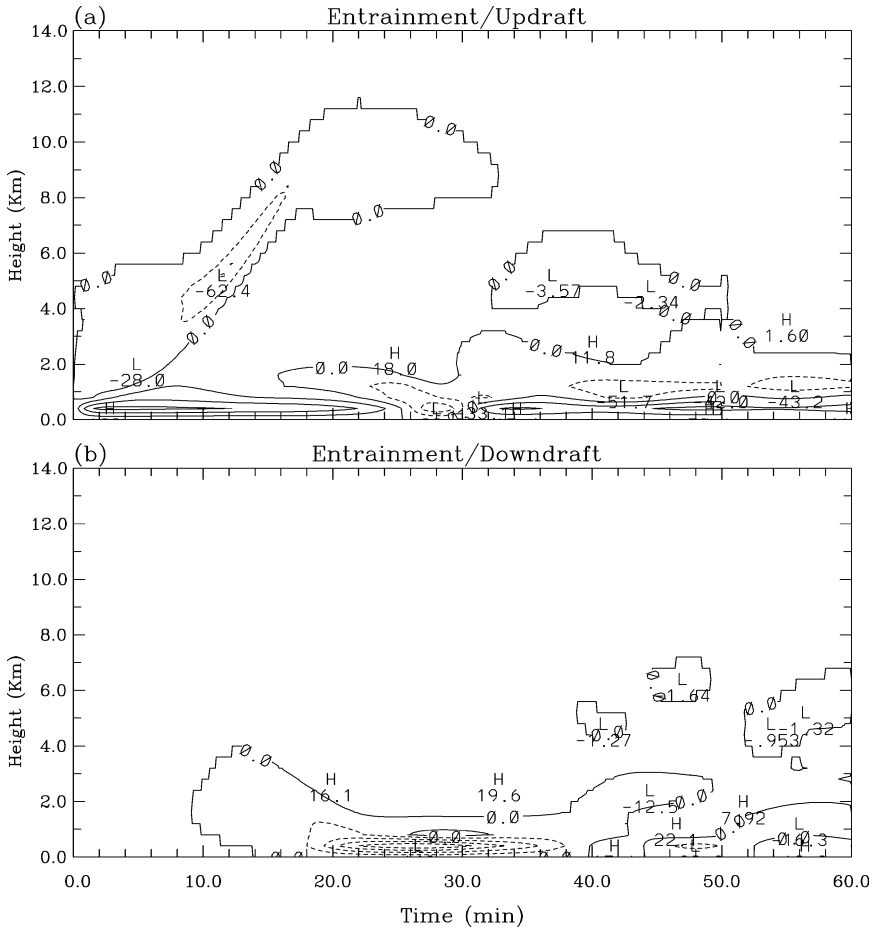

FIG. 9. Time variation of entrainment (positive) and detrainment (negative) rate of nonprecipitable water ($\times 10^6$ kg kg^{-1} s^{-1}), including water vapor, cloud water, and cloud ice (appendix A), from the (a) updraft and (b) downdraft with a contour interval of 20 $\times$ 10^6 kg kg^{-1} s^{-1}.

in a 1D cloud model when it is applied to cumulus parameterization. Except for the radius, which is given, the entrainment–detrainment rate in the ETTM is determined by the continuity equation. In this experiment, a large amount of moisture entrains into lower levels of the updraft (1 $\sim$ 1.5 km depth) and is transported upward (Fig. 9a). Besides moistening the column and being transformed into liquid or solid phases, the rest of the moisture is detrained out of the updraft at upper levels of the cloud (about 3 km deep). Through this process, the moisture can be transported upward and fed back to grid-scale fields in the mesoscale models. After upward motion is replaced by downward motion inside the updraft column, dry air at the middle levels (4 $\sim$ 5 km) can be dragged down and detrained out at low levels (1 $\sim$ 2 km depth). The detrainment rate at low levels in the downdraft column is stronger than the entrainment rate in the updraft column (Fig. 9a versus Fig. 9b) due to a smaller radius and a stronger vertical gradient of the vertical velocity near the surface (Fig. 5a versus Fig. 5b). In other words, the downdraft is more efficient per unit area at bringing middle-level air to low levels than the downward motion in the updraft column (22 to 32 min in Fig. 9).

Figure 10 shows the time variation of the mass flux (F) calculated using the formula

$$F = \rho w B,$$

where B is the updraft–downdraft coverage area. Before 22 min, the mass flux is upward, mainly from the updraft. This induces entrainment (detrainment) at the lower (upper) potion of the updraft cloud (Fig. 9). From 22 to 32 min, the mass flux is upward at upper levels of the cloud, contributed from the updraft, and is downward at lower levels, contributed from both the updraft and downdraft. Therefore, strong detrainment at low levels, weak entrainment at middle levels, and weak detrainment at upper levels are induced. It is worth mentioning again that the total downward flux from the downdraft is weaker due to a smaller coverage area. From these results we can see that the time variation of the entrainment–detrainment process is quite significant, and this implies that the time dependence of subgrid-

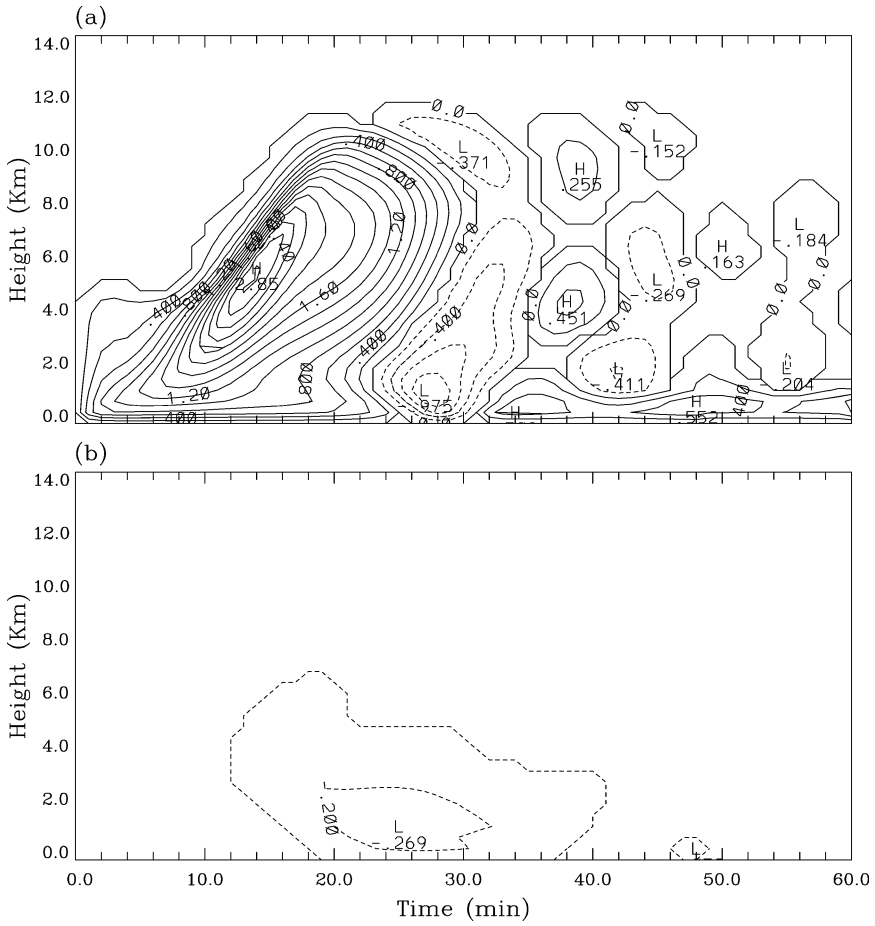

FIG. 10. Time variation of the mass flux ($\times 10^8$ kg s^{-1}) from the (a) updraft and (b) downdraft with a contour interval of 0.2 $\times$ 10^8 kg s^{-1}.

scale cloud effects can be of great importance when the resolution of mesoscale models increases.

The vertical distribution of the total mass flux in Fig. 11 is calculated by integrating the mass flux with time in Fig. 10. The updraft presents a double-peak feature: one at 0.8 km and the other at 4.4 km. The former is dominated by higher densities at lower levels, while the latter is dominated by stronger vertical velocities at upper levels. The downdraft contributes a negative mass flux (downward), particularly under 4 km. At the level of 1.6 km, 39% of the total mass flux is deducted by the downdraft. Therefore, the total mass flux can be reduced significantly through the downdraft process at some lower levels as shown in Fig. 11.

4. Sensitivity tests

a. Environmental sounding

Using a 1D model, Srivastava conducted a series of tests examining the intensity and temperature anomalies in a downdraft (Srivastava 1985, 1987). He found that a microburst downdraft can occur when the environmental lapse rate is large (close to the dry adiabat); otherwise, a large amount of precipitation (rain and/or ice) is required if the environmental lapse rate is relatively small. He also concluded that a cooling is observed only at high rainwater mixing ratio and environmental temperature lapse rate (Srivastava 1985). The issue of cooling regarding the former (i.e., the content of rainwater) is rather complicated due to the involvement of cloud microphysical processes and deserves a separate study. Therefore, we will only examine the environmental sounding in this study.

An experiment is conducted using a modified sounding (thin lines in Fig. 4) from that in section 3 (thick lines in Fig. 4). The relative humidity is kept the same so that the new sounding has a CAPE of 2950 J kg^{-1}, which is close to that in the original sounding (3000 J kg^{-1}). For convenience, we call this new numerical experiment the TADJ case (i.e., temperature adjusted) and the one in section 3 the CNTL case. The lapse rate in the lower atmosphere is larger from TADJ than from CNTL and is close to the dry-adiabatic lapse rate. The numerical setup for TADJ is the same as that in the CNTL case except for the sounding.

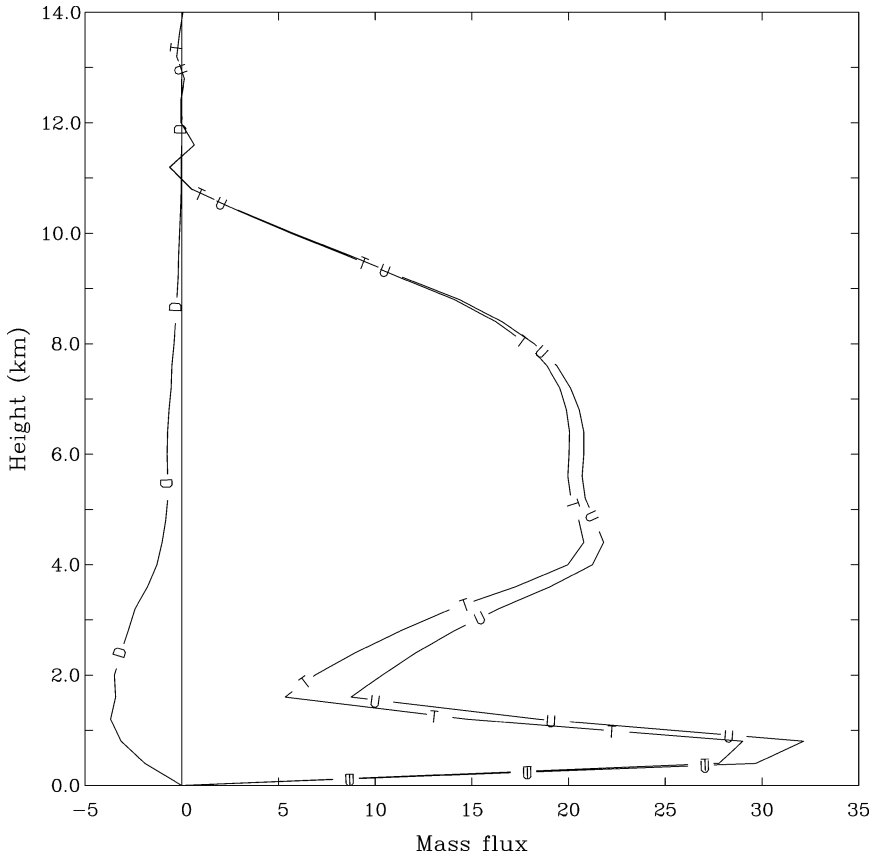

FIG. 11. Vertical distribution of the total mass flux ($\times 10^{10}$ kg) from the updraft (line U), downdraft (line D), and both (line T) within 60 min.

Figures 12a and 12b show the simulated temperature anomaly from the CNTL and TADJ cases, respectively. The maximum temperature anomaly below 2-km height during the downdraft life cycle is 1.41 K (−0.35 K) from the CNTL (TADJ) case. The ETTM is able to produce a cooling in the lower atmosphere from the TADJ case whose lapse rate in the lower atmosphere is larger. This result is consistent with that from Srivastava (1985).

The difference in the cooling and warming between the TADJ and CNTL cases can be partially interpreted from parcel theory. After descent-induced warming, the temperature profile in the unsaturated downdraft will become close to dry adiabatic if neither melting nor evaporative–sublimative cooling occurs. In this situation, if the environmental lapse rate is less than dry adiabatic, the temperature in the downdraft will be warmer than that of the environment. This assumes that the temperature at the origin of the downdraft is the same as that of the environment at the same level. In contrast, if enough hydrometeors are available and they melt and evaporate–sublimate to saturation instantaneously, the temperature profile in the downdraft will become moist adiabatic. In this situation, the temperature in the downdraft can be colder than the environment if the environmental lapse rate is greater than moist adiabatic. Therefore, a cooling–warming of the downdraft relative to its environment is strongly relevant to the melting and evaporative–sublimative rate and the environmental sounding. In the real atmosphere, the temperature profile of the downdraft might not follow the dry adiabat (i.e., microphysical processes are involved) or the moist adiabat (i.e., hydrometeors are not totally evaporated–sublimated) but in between as is shown in Fig. 6. Additionally, the motion in the cloud does not exactly follow parcel theory (see updraft sounding in Fig. 6) as processes like entrainment and lateral eddy diffusion are also involved. In general, however, the larger the environmental lapse rate and the larger the evaporative–sublimative rate of precipitation, the greater the chance for net cooling in the downdraft. Figures 12c and 12d show that the patterns of the rain evaporation rate and their maxima are similar in both cases, a maximum of 5.16×10^{-6} kg kg^{-1} s^{-1} for the CNTL case and 5.24×10^{-6} kg kg^{-1} s^{-1} for the TADJ case. Since the average environment lapse below 2 km is larger in the TADJ case (8.07 K km^{-1}) than in the CNTL case (6.57 K km^{-1}), a cooling near the surface of the downdraft in TADJ but not in CNTL is reason-

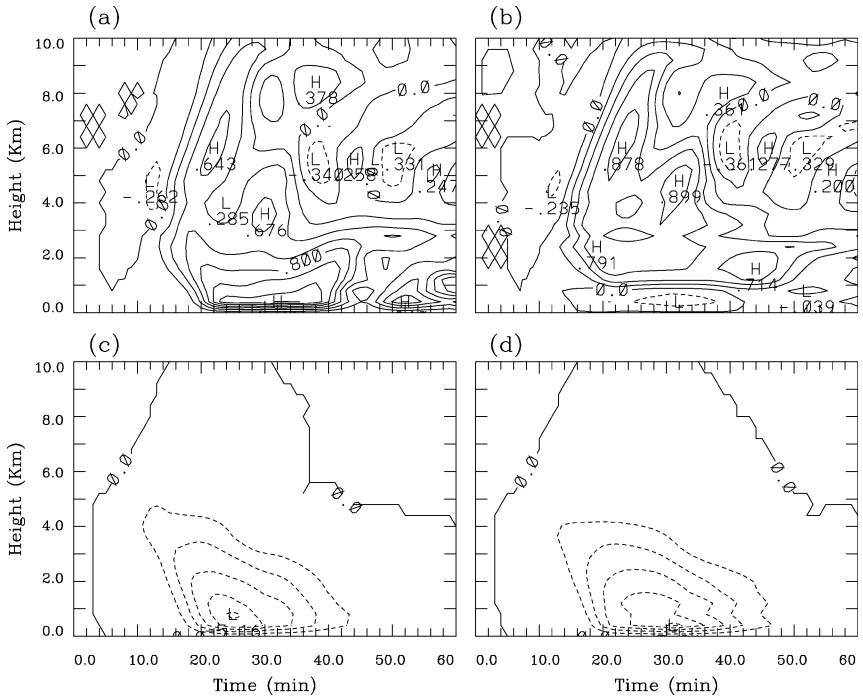

FIG. 12. Time variation of the temperature anomaly (K) in the downdraft from (a) the CNTL case and (b) the TADJ case, and the evaporative rate of rain (kg kg^{-1} s^{-1}) in the downdraft from (c) the CNTL case and (d) the TADJ case. The evaporative rate is multiplied by 1×10^6.

able. Note that the values in Figs. 12c and 12d are negative since it is a loss for the rain field.

b. Tilting angle and radius of the cloud

The tilting angle and radius of the cloud can significantly influence the vertical distribution of the mass flux, total precipitation amount, and strength and life cycle of a cloud. To better understand their impacts on cloud effects, two sensitivity tests are conducted: one for the tilting angle and the other for the radius. In both tests, the initial condition and the moist thermal bubble are the same as those used in the CNTL case (section 3), except for the change of the particular parameter in question. The tilting angle varies from 0° to 70° and the radius of the updraft varies from 1000 to 12 000 m. In all experiments, the radius of the downdraft is 40% of the updraft.

Figure 13a shows the vertical velocities and life cycles of clouds with respect to different tilting angles. When the tilting angle increases, the life cycle slightly increases and then decreases for both the updraft and downdraft if 0° is excluded for the downdraft. The separation of precipitation can decrease (increase) the drag force in the updraft (downdraft) and result in a longer life span. However, the increase of the lateral eddy diffusion due to the tilting effect is unfavorable to cloud development. Therefore, to reach a maximum life cycle, the tilting angles are 10°–20° for the updraft and 20°–25° for the downdraft in this experiment. The maximum strength of the vertical motion decreases in the updraft, and increases and then decreases in the downdraft. When the cloud radius is fixed, greater tilting angles result in larger ratios for the precipitation falling into the downdraft ($1 - R_{in}$). However, the precipitation amount in the updraft decreases with the increase of the tilting angle above 20° (weaker updraft). Therefore, an optimal angle to have the strongest downdraft is 30° in this case study.

The total rainfall amount in the updraft decreases with increasing tilting angle, while for the downdrafts rainfall amounts slightly increase, then decrease (Fig. 13b). As the tilting angle increases from 0° to 10°, the life cycle of the updraft becomes slightly longer, but the total rainfall amount does not necessarily increase since a larger portion of precipitation falls out of the updraft. The total amount from both the updraft and downdraft gives a maximum at 5°. At this angle, the rain rates per unit area from both sources are comparable. As mentioned earlier, the contribution of rainfall amount from the updraft is greater due to the larger coverage area. As the titling angle increases beyond 40°, the contribution of rainfall from the downdraft is more than that from the updraft.

The vertical distribution of total mass flux with respect to tilting angle is shown in Fig. 14. A double peak is still observed for all different angles and the lower peak is still the larger one. Comparing the results from $\alpha_0 = 0°$ and 20° (solid lines), the profiles above 3 km are very close. However, the difference is not negligible

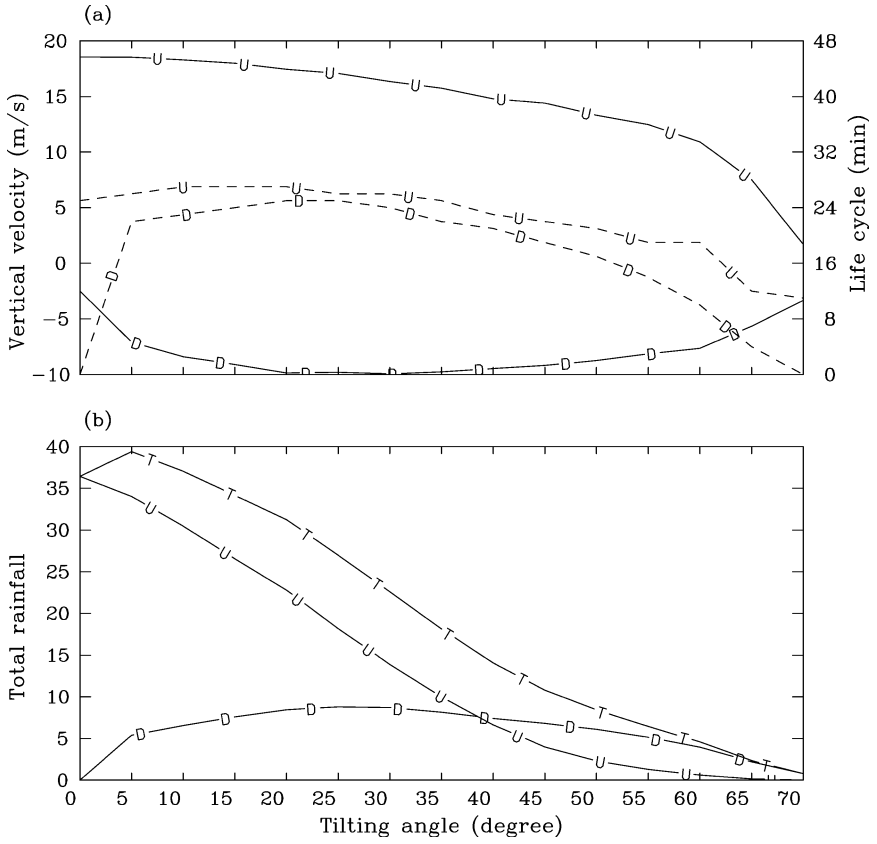

FIG. 13. (a) Maximum upward motion (m s^{-1}) from the updraft (solid line U), the maximum downward motion (m s^{-1}) from the downdraft (solid line D), and the life cycle (min) of the updraft (dashed line U) and downdraft (dashed line D) with respect to different tilting angles. The radius of the downdraft is 40% of that from the updraft. (b) The total accumulated rainfall amount ($\times 10^7$ kg) from the updraft (line U), downdraft (line D), and both (line T) with respect to different tilting angles after a 60-min integration time.

below 3 km. The primary difference is contributed by the downdraft, which reduces the total amount of the vertical mass flux. It is noted that when the tilting angle is less than 20°, the conclusion is similar except that the difference at lower levels gets smaller when the tilting angle is decreased. In essence, the contribution from the downdraft becomes smaller. As the tilting angle becomes greater than 20°, the discrepancy is not only restricted to the lower portion but the upper portion as well. The magnitude of the mass flux is reduced and the cloud becomes shallower as the tilting angle increases. However the upper local maxima almost remain at the same height, except for $\alpha_0 \geq 70°$, which may not be realistic in the real atmosphere.

Figure 15 shows the same information as in Fig. 13 except with respect to different radii of the updraft. When the radius increases, the life cycles for both the updraft and downdraft increase. In Eq. (16), the lateral eddy diffusion term is a momentum sink for cloud development and its influence is proportional to the inverse of the cloud radius. The same equation also shows that entrainment–detrainment is another interaction between the environment and the cloud. Its influence becomes weaker with the increase of the radius because the mixing between the cloud and the environment decreases (Kuo and Raymond 1980). Therefore, when the radius becomes larger, the loss of the vertical momentum due to entrainment–detrainment and due to lateral mixing is reduced.

The maximum vertical velocity in the updraft increases, first sharply, then slowly, when the radius increases from 1000 m to a critical value of 9000 m. After the critical value, the maximum vertical velocity decreases more gradually. A similar conclusion was reached by Kuo and Raymond (1980). It is also noted that an upper bound of the absolute vertical velocity is shown in the downdraft at the radius of 3200 m. In Eq. (22), the radius influences the pressure perturbation directly and the vertical velocity indirectly through the pressure perturbation terms in Eq. (16). The importance of the nonhydrostatic pressure perturbation to cloud development has been demonstrated. Holton (1973) and Chen and Sun (2002) pointed out that the pressure perturbation can weaken the vertical velocity. Moreover,

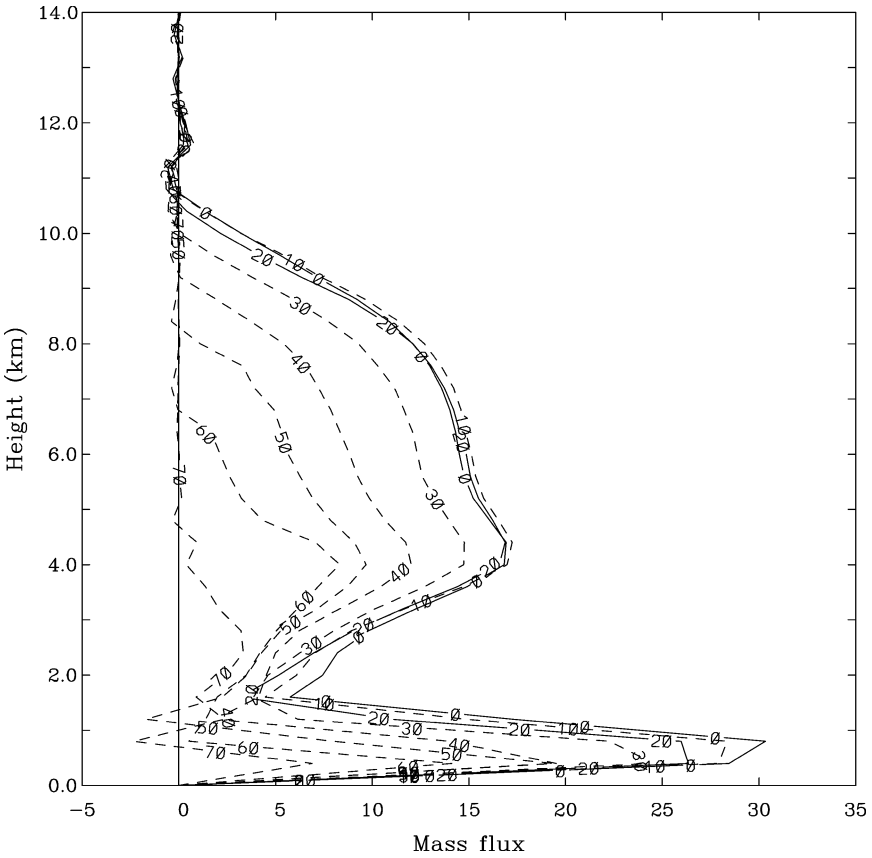

FIG. 14. Vertical distribution of total mass flux ($\times 10^{10}$ kg) from both the updraft and downdraft within 60 min with different tilting angles. The number indicates the tilting angle in the unit of degree. The profiles with the tilting angles of 0° and 20° are plotted with solid lines.

Holton (1973) and Kuo and Raymond (1980) remarked that the impact of the pressure perturbation on cloud development becomes more significant (greater weakening of vertical velocity) with the increase of the radius. The influences of the pressure perturbation can partially explain the existence of an optimal radius for the strength of a cloud, through other nonlinear terms are also very important.

The total rainfall amount nonlinearly increases with the radius and a larger amount is contributed from the updraft since a small tilting angle (20°) is used (see discussion in section 3). However, the contribution from the downdraft is about 30% of the total and it is not negligible.

The vertical distribution of the total mass flux with respect to different updraft radii is shown in Fig. 16. When the radius is increased, the cloud extends higher and the total mass flux increases due to a longer life cycle and a larger vertical velocity. Therefore, large clouds are more efficient at consuming environmental energy. It is interesting that a single peak of the vertical profile is observed for large clouds, while double peaks are clearly shown for small ones. As mentioned earlier, the upper peak is dominated by the vertical velocity, while the lower peak is dominated by the density. When the radius increases, the magnitude of the upper peak grows faster than the lower peak due to the increase of the vertical velocity and becomes dominant after 6000 m. The upper peak, which is located 1–2 km lower than the level of the maximum vertical velocity, keeps growing with the radius and finally merges with the lower peak. It is also interesting to note that the total mass flux below 0.5 km is almost unchanged with the radius.

5. Summary

An explicit, dynamically and physically based, 1D time-dependent tilting cloud model has been developed for use in cumulus parameterization. This 1D model uses tilting cylindrical coordinates (r, θ, Z) that differ from previous studies in that the tilting axis (Z) is not necessary orthogonal to the (r, θ) plane. Consequently, the horizontal axisymmetric assumption within the cloud is more reasonable.

The ETTM consists of an updraft and a downdraft that use the same dynamic and thermodynamic equations. The updraft is initialized using a moist thermal bubble, and the downdraft is then induced by evapo-

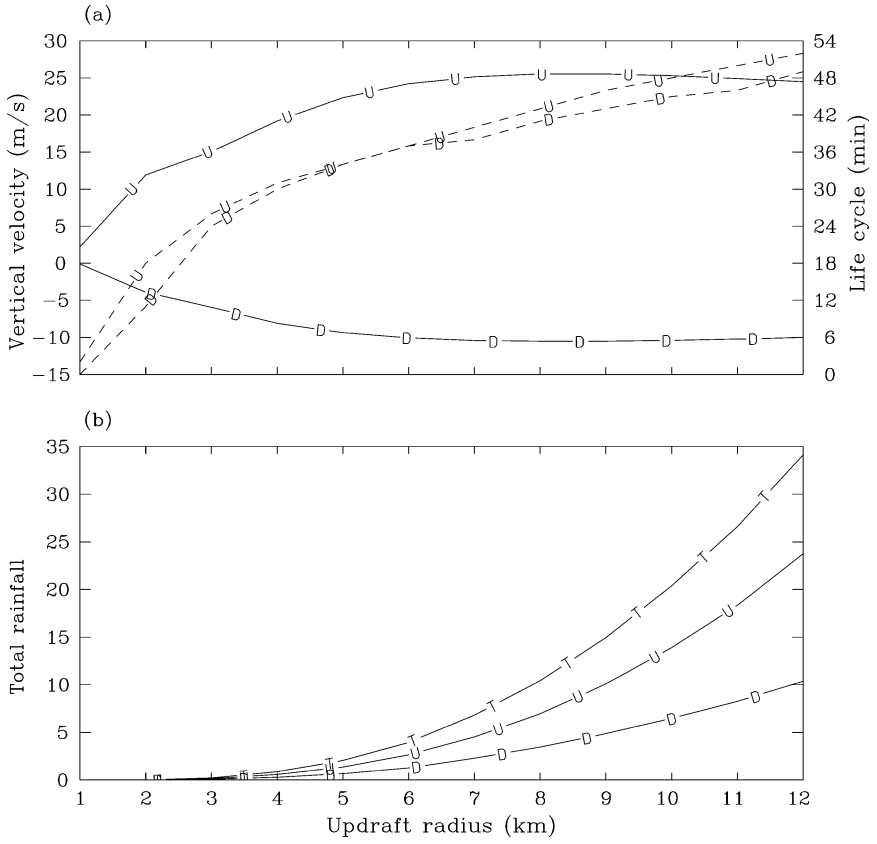

FIG. 15. (a) Maximum upward motion (m s^{-1}) from the updraft (solid line U), the maximum downward motion (m s^{-1}) from the downdraft (solid line D), and the life cycle of the updraft (dashed line U) and downdraft (dashed line D) with respect to different radii of the updraft. The radius of the downdraft is 40% of the updraft. (b) The total accumulated rainfall amount ($\times 10^9$ kg) from the updraft (line U), downdraft (line D), and both (line T) with respect to different radii of the updraft after 60 min of integration time.

rative–sublimative cooling and the drag force of precipitation separating from the updraft instead of arbitrarily initialized. The ratio of precipitation falling out of the updraft depends on the radius of the updraft, tilting angle, and terminal velocity. The radius of the downdraft is assumed to be 40% of the updraft.

An experiment with a 20° tilting angle and a 3000-m radius was conducted as the CNTL case. The preliminary results show that a deep updraft is able to develop along with a coinciding downdraft. In the updraft column, overshooting cooling above the top, evaporative cooling near the surface, and a drying in the lower atmosphere at dissipating stages are well simulated and resemble what is observed naturally. In the downdraft column, a strong wind and a drying at lower levels are generated. However, a warming instead of a cooling in the lower atmosphere is produced. A sensitivity test, the TADJ case, using a modified environmental sounding from the CNTL case, was carried out. The lapse rate of the modified sounding in the lower atmosphere is close to dry adiabatic. With this modified sounding a cooling in the lower troposphere is simulated, and this is consistent with the results of Srivastava (1985). Another simulation with a much higher evaporative cooling rate of rain (6 times of the original rate) was also examined using the sounding from the CNTL case. The result indicates a very weak cooling in the lower atmosphere in the downdraft. Since the microphysical processes are rather complicated, this problem deserves a separate study. We, therefore, leave it for future work.

The skew T–log$p$ diagram shows that the air inside the updraft column is saturated after convection occurs, but the vertical profile does not follow a moist adiabat. In the downdraft, the air is unsaturated during the entire life cycle. In this experiment, a strong downdraft occurs below 4 km, and weak downward motion extends up to 9 km. As a result, the air above 4 km moistens within the downdraft due to evaporation and sublimation. However, it dries below that level due to strong subsidence.

The importance of the downdraft is also examined. The downdraft can significantly reduce the total mass flux at low levels. The precipitation rate in the downdraft can be much higher than that of the updraft, though the total contribution is still smaller than the updraft due to

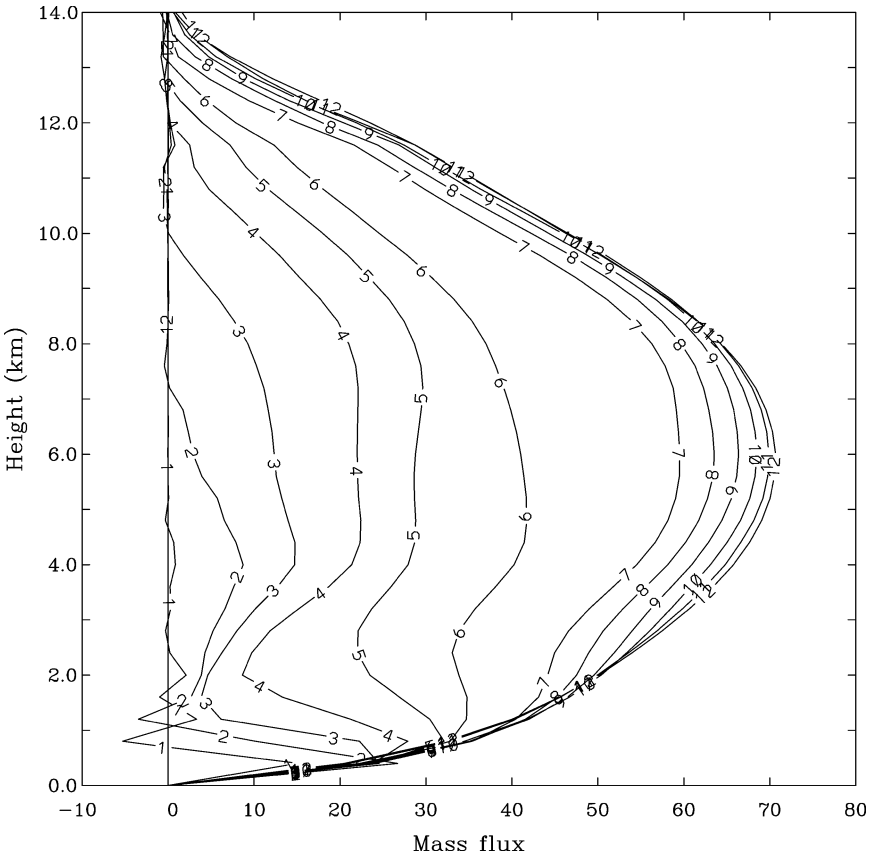

FIG. 16. Vertical distribution of total mass flux ($\times 10^{10}$ kg) from both the updraft and downdraft within 60 min with different radii of the updraft. The number indicates the radius in the unit of km.

a smaller coverage area when the tilting angle is small (less than 40°).

As the resolution of mesoscale numerical models increases, the time dependency of the cloud properties, which is generally ignored, may become important. This study shows that the time variation of the mass flux and entrainment–detrainment rate is quite significant. The time dependence of a 1D cloud model in a cumulus parameterization scheme in high-resolution mesoscale models may need to be considered. The next natural step is to further study these issues by implementing the 1D cloud into a mesoscale model. It is worth mentioning again that the entrainment–detrainment rate is well defined in the ETTM.

To further examine the ETTM, two additional sensitivity tests were conducted, for the tilting angle and the cloud radius. The life cycle, strength, and precipitation amount are very sensitive to these two parameters. At a fixed tilting angle of 20°, the maximum strength of the vertical velocity appears at 9000 m for the updraft and 3200 m for the downdraft in this study. These critical values can be partially explained by the nonhydrostatic pressure perturbation. The pressure perturbation weakens the maximum vertical velocity, and its influence becomes more pronounced with the increase of the radius.

The magnitude and vertical profile of the total mass flux are quite sensitive to the tilting angle and radius. A double-peak feature is simulated when the tilting angle is small (less than 40°). The primary low-level peak is dominated by the density, while the upper-level peak is dominated by the vertical velocity. As the cloud radius increases, the upper peak is enhanced by the vertical velocity and a single-peak feature becomes dominant. When the tilting angle is less than 20°, differences in the upper vertical profiles are negligible. However, differences in the lower profiles in the downdraft are observed. The cloud becomes shallower with a larger tilting angle or with a smaller cloud radius.

The results from this 1D model are quite reasonable and promising, although some improvements are still required. This is a preliminary study of this model with one sounding. More tests with different soundings and comparisons with 3D cloud model results as well as with observations will be conducted to further examine this model. The tilting angle and radius of the updraft–downdraft can significantly influence the vertical distribution of mass flux, the total precipitation amount,

and the strength and life cycle of a cloud. Therefore, the determination of these values becomes very important. The tilting angle, which is strongly correlated to environmental wind shear, and the radius are predetermined in this study. In the future they will be parameterized as large-scale variables using a 3D cloud resolving model. Eventually, this 1D model will be included in a cumulus parameterization scheme and validated with real data using a mesoscale model.

Acknowledgments. The authors would like to thank Dr. Jiun-dar Chern, Dr. James F. Bresch, and S. Low-Nam for their grateful discussions. Further thanks are given to J. Castilleja for converting several figures to eps files.

APPENDIX A

Governing Equations in the Cartesian Coordinates

The following are the governing equations of this cloud model in Cartesian coordinates.

Momentum equations:

$$\frac{\partial u}{\partial t} = -u\frac{\partial u}{\partial x} - v\frac{\partial u}{\partial y} - w\frac{\partial u}{\partial z} - \frac{1}{\rho}\frac{\partial p_{\rm nh}}{\partial x}, \tag{A1}$$

$$\frac{\partial v}{\partial t} = -u\frac{\partial \rho}{\partial x} - v\frac{\partial v}{\partial y} - w\frac{\partial v}{\partial z} - \frac{1}{\rho}\frac{\partial p_{\rm nh}}{\partial y}, \quad \text{and} \tag{A2}$$

$$\frac{\partial w}{\partial t} = -u\frac{\partial w}{\partial x} - v\frac{\partial w}{\partial y} - w\frac{\partial w}{\partial z} - \frac{1}{\rho}\frac{\partial p_{\rm nh}}{\partial z} - g\left(\frac{R_d}{C_p}\right)\frac{p_{\rm nh}}{p_0} - gQ_T, \tag{A3}$$

where u, v, w, ρ, and $-gQ_T$ are velocities in the x, y, and z directions, density, and the drag force due to the weight of precipitation, respectively. The nonhydrostatic pressure ($p_{\rm nh}$) is the pressure deviated from the hydrostatic pressure (p_0).

Thermodynamic equation:

$$\frac{\partial \theta_{\rm ei}}{\partial t} = -u\frac{\partial \theta_{\rm ei}}{\partial x} - v\frac{\partial \theta_{\rm ei}}{\partial y} - w\frac{\partial \theta_{\rm ei}}{\partial z} + \frac{1}{C_p}(L_v q_v - L_f q_i)\frac{d}{dt}\left(\frac{\theta}{T}\right) + \text{micro}(\theta_{\rm ei}), \tag{A4}$$

where $\theta_{\rm ei}$ is called the equivalent ice potential temperature (Chern 1994; Chen and Sun 2002) and is defined as

$$\theta_{\rm ei} = \theta\left[1 + \left(\frac{L_v q_v}{C_p T} - \frac{L_f q_i}{C_p T}\right)\right],$$

where L_v, L_f, T, q_v, and q_i are the latent heat of vaporization and fusion, temperature, and the mixing ratio of water vapor and cloud ice, respectively.

Continuity equation:

$$\frac{\partial u}{\partial x} + \frac{\partial v}{\partial y} + \frac{1}{\rho}\frac{\partial(\rho w)}{\partial z} = 0. \tag{A5}$$

Continuity equations of water substances:

$$\frac{\partial q_x}{\partial t} = -u\frac{\partial q_x}{\partial x} - v\frac{\partial q_x}{\partial y} - w\frac{\partial q_x}{\partial z} + P_x \quad \text{and} \tag{A6}$$

$$\frac{\partial q_y}{\partial t} = -u\frac{\partial q_y}{\partial x} - v\frac{\partial q_y}{\partial y} - w\frac{\partial q_y}{\partial z} + \frac{1}{\rho}\frac{\partial(\rho V_{\rm ty} q_y)}{\partial z} + P_y, \tag{A7}$$

where q_x is the mixing ratio of nonprecipitable water (q_w), cloud water (q_c), or cloud ice, and q_y is the mixing ratio of rain (q_r), snow (q_s), or graupel (q_g). Next, $q_w = q_v + q_c + q_i$, $V_{\rm ty}$ is the terminal velocity of precipitation (rain, snow, or graupel); and P_x and P_y are microphysical production terms of q_x and q_y.

APPENDIX B

Governing Equations in the Axis-Symmetric Tilting Cylindrical Coordinates

Applying the hypothesis that the cloud is horizontally symmetric with respect to the tilting axis ($\partial/\partial\theta = 0$) within the cloud, the equations in the tilting cylindrical coordinates are

$$\frac{\partial \theta_{\rm ei}}{\partial t} = -\frac{1}{r}\frac{\partial(rU\theta_{\rm ei})}{\partial r} - \frac{1}{\rho}\frac{\partial(\rho W\theta_{\rm ei})}{\partial z} + \frac{1}{C_p}(L_v q_v - L_f q_i)\frac{d}{dt}\left(\frac{\theta}{T}\right) + \text{micro}(\theta_{\rm ei}), \tag{B1}$$

$$\frac{1}{r}\frac{\partial(rU)}{\partial r} + \frac{1}{\rho}\frac{\partial(\rho W)}{\partial Z} = 0, \quad \text{and} \tag{B2}$$

$$\frac{\partial q_x}{\partial t} = -\frac{1}{r}\frac{\partial(rUq_x)}{\partial r} - \frac{1}{\rho}\frac{\partial(\rho Wq_x)}{\partial Z} + P_x. \tag{B3}$$

In this model, the divergence equation rather than the momentum equations is used, and it is expressed as

$$\frac{\partial D}{\partial t} = -\frac{1}{r}\frac{\partial(rUD)}{\partial r} - \frac{1}{\rho}\frac{\partial(\rho WD)}{\partial Z} - D^2 + 2\frac{U}{r}\frac{\partial U}{\partial r} - \frac{\partial U}{\partial Z}\frac{\partial W}{\partial r} - \frac{1}{r}\frac{\partial}{\partial r}\left(\frac{r}{\rho}\frac{\partial p_{\rm nh}}{\partial r}\right) - a\cos\theta\frac{1}{r}\frac{\partial}{\partial r}(rB) + ab\frac{\cos\theta}{r\rho}\frac{\partial}{\partial r}\left(r\frac{\partial p_{\rm nh}}{\partial Z}\right) - a^2\frac{\cos^2\theta}{\rho}\left[\frac{1}{r}\frac{\partial}{\partial r}\left(r\frac{\partial p_{\rm nh}}{\partial r}\right)\right], \tag{B4}$$

where D is the divergence field in the tilting coordinates and its formula is

$$D = \frac{1}{r}\frac{\partial(rU)}{\partial r}. \tag{B5}$$

REFERENCES

Anthes, R. A., 1977: A cumulus parameterization scheme utilizing a one-dimensional cloud model. *Mon. Wea. Rev.*, **105,** 270–286.

Arakawa, A., and W. Schubert, 1974: Interaction of a cumulus cloud ensemble with the large-scale environment, Part I. *J. Atmos. Sci.*, **31,** 674–701.

Asai, T., and A. Kasahara, 1967: A theoretical study of the compensating downward motions associated with cumulus clouds. *J. Atmos. Sci.*, **24,** 487–496.

Betts, A. K., 1986: New convective adjustment scheme. Part I. Observational and theoretical basis. *Quart. J. Roy. Meteor. Soc.*, **112,** 677–691.

Brown, J. M., 1979: Mesoscale unsaturated downdrafts driven by rainfall evaporation: A numerical study. *J. Atmos. Sci.*, **36,** 313–338.

Chen, S.-H., and W.-Y. Sun, 2002: A one-dimensional time dependent cloud model. *J. Meteor. Soc. Japan*, **80,** 99–118.

Cheng, M.-D., 1989a: Effects of downdrafts and mesoscale convective organization on the heat and moisture budgets of tropical cloud clusters. Part I: A diagnostic cumulus ensemble model. *J. Atmos. Sci.*, **46,** 1517–1538.

——, 1989b: Effects of downdrafts and mesoscale convective organization on the heat and moisture budgets of tropical cloud clusters. Part II: Effects of convective downdrafts. *J. Atmos. Sci.*, **46,** 1540–1564.

Chern, D. C., 1994: Numerical simulations of cyclogenesis over the western United States. Ph.D. thesis, Purdue University, 178 pp.

Emanuel, K. A., 1991: A scheme for representing cumulus convection in large-scale models. *J. Atmos. Sci.*, **48,** 2313–2335.

Ferrier, B. S., and R. A. Houze, 1989: One-dimensional time-dependent modeling of GATE cumulonimbus convection. *J. Atmos. Sci.*, **46,** 330–352.

Frank, W. M., and C. Cohen, 1985: Properties of tropical cloud ensembles estimated using a cloud model and an observed updraft population. *J. Atmos. Sci.*, **42,** 1911–1928.

Fritsch, J. M., and C. F. Chappell, 1980: Numerical prediction of convectively driven mesoscale pressure systems. Part I: Convective parameterization. *J. Atmos. Sci.*, **37,** 1722–1733.

Grabowski, W. W., 2001: Coupling cloud processes with the large-scale dynamics using the cloud-resolving convection parameterization. *J. Atmos. Sci.*, **58,** 978–997.

Gray, M. E. B., 2000: Characteristics of numerically simulated mesoscale convective systems and their application to parameterization. *J. Atmos. Sci.*, **57,** 3953–3970.

Grell, G. A., 1993: Prognostic evaluation of assumptions used by cumulus parameterizations. *Mon. Wea. Rev.*, **121,** 764–787.

——, Y.-H. Kuo, and R. J. Pasch, 1991: Semiprognostic tests of cumulus parameterization schemes in the middle latitudes. *Mon. Wea. Rev.*, **119,** 5–31.

Haines, P. A., and W. Y. Sun, 1994: A convective cloud model for use in a cumulus parameterization scheme. *Mon. Wea. Rev.*, **122,** 165–182.

Holton, J. R., 1973: A one-dimensional cumulus model including pressure perturbations. *Mon. Wea. Rev.*, **101,** 201–205.

Hu, Q., 1997: A cumulus parameterization based on a cloud model of intermittently rising thermals. *J. Atmos. Sci.*, **54,** 2292–2307.

Kain, J. S., and J. M. Fritsch, 1990: A one-dimensional entraining/detraining plume model and its application in convective parameterization. *J. Atmos. Sci.*, **47,** 2784–2802.

——, and J. M. Fritsch, 1993: Convective parameterization for mesoscale models: The Kain–Fritsch scheme. *The Representation of Cumulus Convection in Numerical Models, Meteor. Monogr.*, No. 46, Amer. Meteor. Soc., 165–170.

Khairoutdinov, M. F., and D. A. Randall, 2001: A cloud-resolving model as a cloud parameterization in the NCAR Community Climate System model: Preliminary results. *Geophys. Res. Lett.*, **28,** 3617–3620.

Kreitzberg, C. W., and D. J. Perkey, 1976: Release of potential instability. Part I: A sequential plume model within a hydrostatic primitive equation model. *J. Atmos. Sci.*, **33,** 456–475.

Kuo, H. L., 1965: On formation and intensification of tropical cyclones through latent heat release by cumulus convection. *J. Atmos. Sci.*, **22,** 40–63.

——, 1974: Further studies of the parameterization of the influence of cumulus convection on large-scale flow. *J. Atmos. Sci.*, **31,** 1232–1240.

——, and W. H. Raymond, 1980: A quasi-one-dimensional cumulus cloud model and parameterization of cumulus heating and mixing effects. *Mon. Wea. Rev.*, **108,** 991–1009.

Lemone, M. A., and E. J. Zipser, 1980: Cumulonimbus vertical velocity events in GATE. Part I: Diameter, intensity and mass flux. *J. Atmos. Sci.*, **37,** 2444–2457.

Lin, Y.-L., R. D. Farley, and H. D. Orville, 1983: Bulk parameterization of the snow field in a cloud model. *J. Climate Appl. Meteor.*, **22,** 1065–1092.

Liu, C., M. W. Moncrieff, and W. W. Grabowski, 2001: Explicit and parameterized realizations of convective cloud systems in TOGA COARE. *Mon. Wea. Rev.*, **129,** 1689–1703.

Manabe, S., J. Smagorinsky, and R. F. Strickler, 1965: Simulated climatology of a general circulation model with a hydrological cycle. *Mon. Wea. Rev.*, **93,** 769–798.

Molinari, J., 1982: A method for calculating the effects of deep cumulus convection in numerical models. *Mon. Wea. Rev.*, **110,** 1527–1534.

——, and T. Corsetti, 1985: Incorporation of cloud-scale and mesoscale downdrafts into a cumulus parameterization: Results of one- and three-dimensional integrations. *Mon. Wea. Rev.*, **113,** 485–501.

Moncrieff, M. W., 1981: A theory of organized steady convection and its transport properties. *Quart. J. Roy. Meteor. Soc.*, **107,** 29–50.

——, 1992: Organized convective systems: Archetypal dynamical models, mass and momentum flux theory, and parameterization. *Quart. J. Roy. Meteor. Soc.*, **118,** 819–850.

Nitta, T., 1975: Observational determination of cloud mass flux distributions. *J. Atmos. Sci.*, **32,** 73–91.

Ogura, Y., and T. Takahashi, 1971: Numerical simulation of the life cycle of a thunderstorm cell. *Mon. Wea. Rev.*, **99,** 895–911.

Ooyama, K., 1971: A theory of parameterization of cumulus convection. *J. Meteor. Soc. Japan*, **49,** 744–756.

Rutledge, S. A., and P. V. Hobbs, 1984: The mesoscale and microscale structure and organization of clouds and precipitation in midlatitude cyclones. XII: A diagnostic modeling study of precipitation development in narrow cold-frontal rainbands. *J. Atmos. Sci.*, **41,** 2949–2972.

Schlesinger, R. E., 1978: A three-dimensional numerical model of an isolated thunderstorm. Part I: Comparative experiments for variable ambient wind shear. *J. Atmos. Sci.*, **35,** 690–713.

Srivastava, R. C., 1985: A simple model of evaporatively driven downdraft: Application to microburst downdraft. *J. Atmos. Sci.*, **42,** 1004–1023.

——, 1987: A model of intense downdrafts driven by the melting and evaporation of precipitation. *J. Atmos. Sci.*, **44,** 1752–1773.

Sun, W. Y., 1984: Numerical analysis for hydrostatic and nonhydrostatic equations of inertial-internal gravity waves. *Mon. Wea. Rev.*, **112,** 259–268.

——, and P. A. Haines, 1996: Semi-prognostic tests of a new mesoscale cumulus parameterization scheme. *Tellus*, **48A,** 272–289.

Tiedtke, M., 1989: A comprehensive mass flux scheme for cumulus parameterization in large-scale models. *Mon. Wea. Rev.*, **117,** 1779–1800.

Wang, J., and D. A. Randall, 1996: A cumulus parameterization based on the generalized convective available potential energy. *J. Atmos. Sci.*, **53,** 716–727.